## Simultaneous observations of the blazar PKS 2155-304 from ultra-violet to TeV energies

Abdalla, H.; Berge, D.; Bryan, M.; Prokhorov, D.A.; Prokoph, H.; Simoni, R. ; Vink, J.; H.E.S.S. Collaboration

[Link to publication](Link to publication)

**Astronomy & Astrophysics**

# Simultaneous observations of the blazar PKS 2155−304 from ultra-violet to TeV energies

H. Abdalla[1], R. Adam[26], F. Aharonian[3,4,5], F. Ait Benkhali[3], E. O. Angüner[19], M. Arakawa[37], C. Arcaro[1],
C. Armand[22], H. Ashkar[17], M. Backes[8,1], V. Barbosa Martins[33], M. Barnard[1], Y. Becherini[10], D. Berge[33],
K. Bernlöhr[3], R. Blackwell[13], M. Böttcher[1], C. Boisson[14], J. Bolmont[15], S. Bonnefoy[33], J. Bregeon[16], M. Breuhaus[3],
F. Brun[17], P. Brun[17], M. Bryan[9], M. Büchele[32], T. Bulik[18], T. Bylund[10], S. Caroff[15], A. Carosi[22], S. Casanova[20,3],
M. Cerruti[15,42,★], T. Chand[1], S. Chandra[1], A. Chen[21], S. Colafrancesco[21], M. Curyło[18], I. D. Davids[8], C. Deil[3],
J. Devin[24], P. deWilt[13], L. Dirson[2], A. Djannati-Ataï[27], A. Dmytriiev[14], A. Donath[3], V. Doroshenko[25], J. Dyks[30],
K. Egberts[31], G. Emery[15], J.-P. Ernenwein[19], S. Eschbach[32], K. Feijen[13], S. Fegan[26], A. Fiasson[22], G. Fontaine[26],
S. Funk[32], M. Füßling[33], S. Gabici[27], Y. A. Gallant[16], F. Gaté[22], G. Giavitto[33], L. Giunti[27], D. Glawion[23],
J. F. Glicenstein[17], D. Gottschall[25], M.-H. Grondin[24], J. Hahn[3], M. Haupt[33], G. Heinzelmann[2], G. Henri[28],
G. Hermann[3], J. A. Hinton[3], W. Hofmann[3], C. Hoischen[31], T. L. Holch[7], M. Holler[12], D. Horns[2], D. Huber[12],
H. Iwasaki[37], M. Jamrozy[34], D. Jankowsky[32], F. Jankowsky[23], A. Jardin-Blicq[3], I. Jung-Richardt[32],
M. A. Kastendieck[2], K. Katarzyński[35], M. Katsuragawa[38], U. Katz[32], D. Khangulyan[37], B. Khélifi[27], J. King[23],
S. Klepser[33], W. Kluźniak[30], Nu. Komin[21], K. Kosack[17], D. Kostunin[33], M. Kreter[1], G. Lamanna[22], A. Lemière[27],
M. Lemoine-Goumard[24], J.-P. Lenain[15], E. Leser[31,33], C. Levy[15], T. Lohse[7], I. Lypova[33], J. Mackey[4], J. Majumdar[33],
D. Malyshev[25], V. Marandon[3], A. Marcowith[16], A. Mares[24], C. Mariaud[26], G. Martí-Devesa[12], R. Marx[3],
G. Maurin[22], P. J. Meintjes[36], A. M. W. Mitchell[3,41], R. Moderski[30], M. Mohamed[23], L. Mohrmann[32], C. Moore[29],
E. Moulin[17], J. Muller[26], T. Murach[33], S. Nakashima[40], M. de Naurois[26], H. Ndiyavala[1], F. Niederwanger[12],
J. Niemiec[20], L. Oakes[7], P. O'Brien[29], H. Odaka[39], S. Ohm[33], E. de Ona Wilhelmi[33], M. Ostrowski[34], I. Oya[33],
M. Panter[3], R. D. Parsons[3], C. Perennes[15], P.-O. Petrucci[28], B. Peyaud[17], Q. Piel[22], S. Pita[27], V. Poireau[22],
A. Priyana Noel[34], D. A. Prokhorov[21], H. Prokoph[33], G. Pühlhofer[25], M. Punch[27,10], A. Quirrenbach[23], S. Raab[32],
R. Rauth[12], A. Reimer[12], O. Reimer[12], Q. Remy[16], M. Renaud[16], F. Rieger[3], L. Rinchiuso[17], C. Romoli[3,★],
G. Rowell[13], B. Rudak[30], E. Ruiz-Velasco[3], V. Sahakian[6], S. Sailer[3], S. Saito[37], D. A. Sanchez[22,★], A. Santangelo[25],
M. Sasaki[32], R. Schlickeiser[11], F. Schüssler[17], A. Schulz[33], H. M. Schutte[1], U. Schwanke[7], S. Schwemmer[23],
M. Seglar-Arroyo[17], M. Senniappan[10], A. S. Seyffert[1], N. Shafi[21], K. Shiningayamwe[8], R. Simoni[9], A. Sinha[27],
H. Sol[14], A. Specovius[32], M. Spir-Jacob[27], Ł. Stawarz[34], R. Steenkamp[8], C. Stegmann[31,33], C. Steppa[31],
T. Takahashi[38], T. Tavernier[17], A. M. Taylor[33], R. Terrier[27], D. Tiziani[32], M. Tluczykont[2], C. Trichard[26], M. Tsirou[16],
N. Tsuji[37], R. Tuffs[3], Y. Uchiyama[37], D. J. van der Walt[1], C. van Eldik[32], C. van Rensburg[1], B. van Soelen[36],
G. Vasileiadis[16], J. Veh[32], C. Venter[1], P. Vincent[15], J. Vink[9], H. J. Völk[3], T. Vuillaume[22,★], Z. Wadiasingh[1],
S. J. Wagner[23], R. White[3], A. Wierzcholska[20,23], R. Yang[3], H. Yoneda[38], M. Zacharias[1], R. Zanin[3], A. A. Zdziarski[30],
A. Zech[14], J. Zorn[3], N. Żywucka[1],
and
G. M. Madejski[43,★], K. Nalewajko[30], K. K. Madsen[44], J. Chiang[43], M. Baloković[50,51], D. Paneque[55], A. K. Furniss[45],
M. Hayashida[37], C. M. Urry[46], M. Ajello[47], F. A. Harrison[44], B. Giebels[26], D. Stern[48], K. Forster[44], P. Giommi[52],
M. Perri[52,53,★], S. Puccetti[52], A. Zoglauer[49], and G. Tagliaferri[54]

*(Affiliations can be found after the references)*

**ABSTRACT**

Here we report the results of the first ever contemporaneous multi-wavelength observation campaign on the BL Lac object PKS 2155−304 involving *Swift*, *NuSTAR*, *Fermi*-LAT, and H.E.S.S. The use of these instruments allows us to cover a broad energy range, which is important for disentangling the different radiative mechanisms. The source, observed from June 2013 to October 2013, was found in a low flux state with respect to previous observations but exhibited highly significant flux variability in the X-rays. The high-energy end of the synchrotron spectrum can be traced up to 40 keV without significant contamination by high-energy emission. A one-zone synchrotron self-Compton model was used to reproduce the broadband flux of the source for all the observations presented here but failed for previous observations made in April 2013. A lepto-hadronic solution was then explored to explain these earlier observational results.

**Key words.** BL Lacertae objects: individual: PKS 2155−304 – astroparticle physics

---

# 1. Introduction

Blazars are active galactic nuclei (AGNs) with an ultra-relativistic jet pointing towards the Earth. The spectral energy distribution (SED) of blazars exhibits two distinct bumps. The low-energy part (from radio to X-ray) is attributed to synchrotron emission while there is still debate on the emission process responsible for the high-energy bump (from X-ray up to TeV). Synchrotron self-Compton (SSC) models reproduce such emission invoking only leptons. The photons are then produced via synchrotron emission and inverse-Compton scattering. Hadronic blazar models, in which the high-energy component of the blazar SED is ascribed to emission by protons in the jet, or by secondary leptons produced in $p-\gamma$ interactions, have been widely studied (see e.g. Mannheim 1993; Aharonian 2000; Mücke & Protheroe 2001) as an alternative to leptonic models. These latter convey a certain advantage in that they provide a link between photon, cosmic-ray, and neutrino emission from AGNs, and thus open the multi-messenger path to study AGN jets as cosmic-ray accelerators. Interest in hadronic blazar models has recently increased with the first hint (at $3\sigma$ level) of an association of an IceCube high-energy neutrino with the flaring $\gamma$-ray blazar TXS 0506+056 (IceCube Collaboration 2018).

To distinguish between the different models, accurate and contemporaneous observations over a wide energy range are of utmost importance. These are possible with the Nuclear Spectroscopic Telescope Array (*NuSTAR*) launched in 2012, which permits more sensitive studies above 10 keV than previous X-ray missions. Its sensitivity in hard X-rays up to 79 keV enables an examination of the high-energy end of the synchrotron emission even in high-frequency peaked BL Lac (HBL) objects. Such emission is produced by electrons with the highest Lorentz factors, which could be responsible for the $\gamma$-ray emission above tens of GeV that can be detected by ground-based facilities such as the High Energy Stereoscopic System (H.E.S.S.).

One of the best-suited objects for joint observations is PKS 2155−304 ($z = 0.116$, Falomo et al. 1993), a well-known southern object classified as an HBL with HEAO-1 observations in X-rays (Schwartz et al. 1979). The source is a bright and variable $\gamma$-ray emitter. Variability with a timescale of about one month was reported in the GeV energy range by the *Fermi*-Large Area Telescope (LAT; Acero et al. 2015) as well as variations on timescales of approximately one day and rapid flaring events (Cutini 2014, 2013). First detected at TeV energies by Chadwick et al. (1999) in 1996 with the Durham Mark 6 atmospheric Cerenkov telescope, PKS 2155−304 has been regularly observed by H.E.S.S. since the beginning of H.E.S.S. operations, allowing detailed studies of the source variability (H.E.S.S. Collaboration 2017a; Chevalier et al. 2019). The TeV flux of the object exhibits log-normal flux variability behaviour across the whole energy range (H.E.S.S. Collaboration 2017a; Chevalier et al. 2019) making its flux level and variability unpredictable with possible huge flaring events in TeV (Aharonian et al. 2007).

An interesting aspect of this object is the fact that several authors (Zhang 2008; Foschini et al. 2008; Madejski et al. 2016) reported possible contamination of the hard X-ray spectra by the high-energy component (referred to as the hard tail hereafter), but unfortunately, no very high-energy (VHE, $E > 100$ GeV) data were taken at that time to further constrain the VHE $\gamma$-ray flux. Only one multi-wavelength campaign has been conducted so far, using X-ray instruments, *Fermi*-LAT, and H.E.S.S. (Aharonian et al. 2009). The gathered data were equally well reproduced by either a leptonic model such as the SSC model (Aharonian et al. 2009) or a lepto-hadronic model (Cerruti et al. 2012).

PKS 2155−304 was subsequently the target of a multi-wavelength campaign from June to October 2013 by *NuSTAR*, H.E.S.S., the *Neil Gehrels Swift* Observatory, and *Fermi*-LAT. These instruments observed PKS 2155−304 to provide contemporaneous data for the first time in a very broad energy range, extending from ultra-violet up to TeV $\gamma$-rays and yielding a more complete coverage in the X-ray and $\gamma$-ray ranges than the previous campaign held in 2008 (Aharonian et al. 2009).

This paper presents the gathered multi-wavelength data from the 2013 campaign and an analysis of these data in Sect. 2. In Sect. 3, the variability of the source and the X-ray spectra are discussed. Section 4 presents the modeling of the data, and Sect. 5 summarizes the findings of this campaign.

# 2. Data analysis

PKS 2155−304 is an important calibration source in X-rays and was observed during a cross-calibration campaign with other X-ray instruments early in the *NuSTAR* mission (Madsen et al. 2017). The multi-wavelength observations of the source in April 2013 including *NuSTAR*, *XMM-Newton*, and *Fermi*-LAT were reported by Madejski et al. (2016), and those are denoted "epoch 0" in this paper. Observations of PKS 2155−304 were made as part of the "Principal Investigator" phase of the *NuSTAR* mission. The aim was to have those observations take place in exact coincidence with observations by the $\gamma$-ray observatory H.E.S.S. Because of diverse constraints (technical problems, bad weather, etc.), H.E.S.S., *NuSTAR*, and *Swift* only observed PKS 2155−304 simultaneously during four epochs, where each epoch corresponds to observations conducted on a given night (2013-07-17, 2013-08-03, 2013-08-08, and 2013-09-28), labelled as epochs 1, 2, 3, and 4. Both H.E.S.S. and *Swift* observed the blazar for two additional epochs (2013-06-05 and 2013-06-19; labelled 5 and 6). Epoch 6 is presented for sake of completeness since the *Swift* data were found to be unusable (see Sect. 2.4). *NuSTAR* and *Swift* also observed PKS 2155−304 during three extra epochs (labelled 7, 8, and 9): those are also reported here for the sake of completeness. For each epoch, *Fermi*-LAT data were analysed and the results are reported in Sect. 2.2. Figure 1 presents the overall light curve derived from all the epochs.

## 2.1. H.E.S.S. data analysis and results

The H.E.S.S. array is located in the Khomas Highland, in Namibia (23°16′18″ S, 16°30′01″ E), at an altitude of 1800 m above sea level. Now in its second phase, H.E.S.S., is an array of five imaging Atmospheric Cherenkov telescopes. Four of the telescopes (CT1-4) have segmented optical reflectors of 12 m in diameter consisting of 382 mirrors (Bernlöhr et al. 2003) and cameras composed of 960 photomultipliers. Together these form the array of the H.E.S.S. phase I. The second phase started in September 2012 with the addition of a 28 m diameter telescope (CT5) with a camera of 2048 photomultipliers in the centre of the array. The system operates either in Stereo mode, requiring the detection of an air shower by at least two telescopes (Funk et al. 2004; Holler et al. 2015), or in Mono mode in which the array triggers on events detected only with CT5.

PKS 2155−304 was observed by the full H.E.S.S. phase II array during the present observational campaign. Table 1 gives the date of each observation and the results of the analysis described in the following sections. To ensure good data quality,
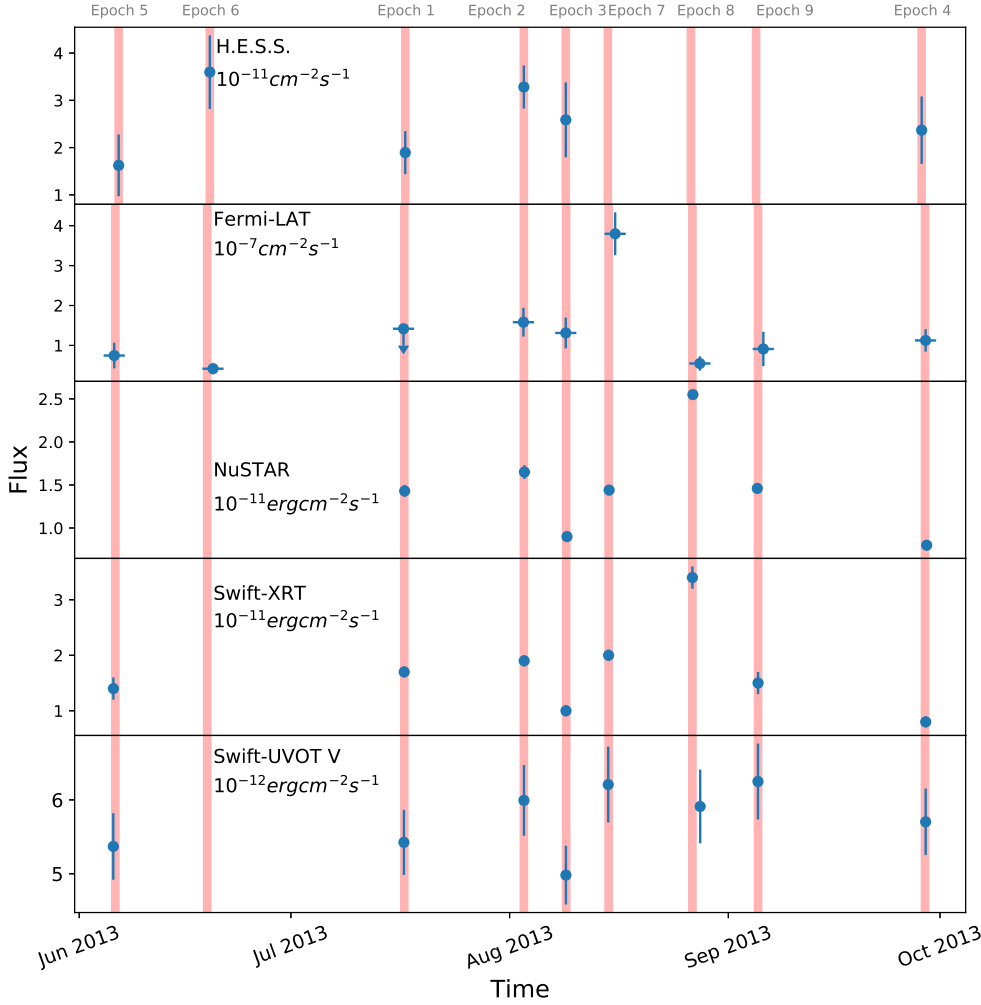
**Fig. 1.** Multiwavelength light curve of PKS 2155−304 in (*from top to bottom*) TeV, GeV, X-ray, and UV. The red lines illustrate the epochs mentioned in the text.

**Table 1.** H.E.S.S. observations of PKS 2155−304.

| Epoch | Date | Live time [h] | Mode | $E_{th}$ [TeV] | $\phi_{dec}(E_{dec})$ [$10^{-12}$ cm$^{-2}$ s$^{-1}$ TeV$^{-1}$] | $\Gamma$ | $E_{dec}$ [TeV] | Flux [$10^{-12}$ cm$^{-2}$ s$^{-1}$] |
|---|---|---|---|---|---|---|---|---|
| 1 | 2013-07-17 | 1.2 | Stereo | 0.108 | $68.1 \pm 5.5$ | $2.89 \pm 0.12$ | 0.27 | $57.6 \pm 5.4$ |
| 2 | 2013-08-03 | 2.0 | Mono | 0.072 | $324.8 \pm 27.7$ | $2.84 \pm 0.14$ | 0.18 | $173.4 \pm 17.2$ |
| 3 | 2013-08-08 | 0.4 | Stereo | 0.120 | $98.9 \pm 11.6$ | $2.82 \pm 0.21$ | 0.26 | $59.1 \pm 7.5$ |
| 4 | 2013-09-28 | 1.2 | Mono | 0.072 | $211.5 \pm 28.5$ | $2.72 \pm 0.23$ | 0.20 | $133.4 \pm 20.9$ |
| 5 | 2013-06-05 | 0.9 | Stereo | 0.146 | $61.8 \pm 12.3$ | $3.17 \pm 0.60$ | 0.26 | $27.0 \pm 5.8$ |
| 6 | 2013-06-19 | 0.8 | Stereo | 0.108 | $123.1 \pm 9.1$ | $2.79 \pm 0.13$ | 0.26 | $90.1 \pm 7.8$ |
| Stack | | 6.5 | Combined | 0.121 | $75.7 \pm 2.7$ | $3.00 \pm 0.06$ | 0.29 | $62.0 \pm 2.6$ |

**Notes.** The first five columns give the epoch label, the observation date, the live time, the observation mode, and the energy threshold. The data were fitted with a simple power-law with differential flux $\phi_{dec}$ at $E_{dec}$ (the decorrelation energy) and with an index $\Gamma$. The integrated flux above $E_{th}$ is also given.

each observation of 28 min had to pass standard quality criteria (Aharonian et al. 2006). For two nights (2013-08-03 and 2013-09-28; epochs 2 and 4), these criteria were not met by the four 12 m telescopes. Therefore, only CT5 Mono observations are available for these nights.

Data for each night were analysed independently using the Model analysis (de Naurois & Rolland 2009) adapted for the five-telescope array ("Stereo analysis" hereafter). In this case, `Loose cuts` (with a threshold of 40 photo-electrons) were used to lower the energy threshold. For the Mono analysis, `standard`

`cuts` (threshold of 60 photo-electrons) were applied to minimize systematic uncertainties.

The spectra obtained at each epoch were extracted using a forward-folding method described in Piron et al. (2001). For each night, a power-law model was used of the form $\phi_{dec}(E/E_{dec})^{-\Gamma}$, where $E_{dec}$ is the decorrelation energy. Table 1 lists the parameters providing the best fits to the data above an energy threshold $E_{th}$. This threshold is defined as the energy where the acceptance is 10% of the maximal acceptance.

**Table 2.** *Fermi*-LAT observations of PKS 2155−304.

| Epoch | Date | TS | $\phi_{\mathrm{dec}}(E_{\mathrm{dec}})$ [$10^{-12}$ cm$^{-2}$ s$^{-1}$ MeV$^{-1}$] | $\Gamma$ | $E_{\mathrm{dec}}$ [MeV] | Flux [$10^{-8}$ ph cm$^{-2}$ s$^{-1}$] |
|---|---|---|---|---|---|---|
| 1 | 2013-07-17 | 19.8 | | | | <14.2 |
| 2 | 2013-08-03 | 131.1 | $16.2 \pm 3.4$ | $1.99 \pm 0.17$ | 909 | $15.8 \pm 3.6$ |
| 3 | 2013-08-08 | 99.8 | $18.5 \pm 5.4$ | $2.01 \pm 0.26$ | 845 | $13.1 \pm 3.8$ |
| 4 | 2013-09-28 | 154.6 | $9.3 \pm 1.7$ | $1.79 \pm 0.13$ | 1280 | $11.3 \pm 2.8$ |
| 5 | 2013-06-05 | 57.8 | $5.6 \pm 1.5$ | $1.93 \pm 0.22$ | 1260 | $7.5 \pm 3.2$ |
| 6 | 2013-06-19 | 127.0 | $0.9 \pm 0.3$ | $1.38 \pm 0.14$ | 4340 | $4.2 \pm 1.4$ |
| 7 | 2013-08-14 | 295.1 | $124.0 \pm 14.8$ | $2.07 \pm 0.10$ | 540 | $39.0 \pm 5.4$ |
| 8 | 2013-08-26 | 163.1 | $1.1 \pm 0.3$ | $1.48 \pm 0.14$ | 3990 | $5.5 \pm 1.8$ |
| 9 | 2013-09-04 | 46.1 | $6.5 \pm 1.8$ | $2.02 \pm 0.26$ | 1160 | $9.1 \pm 4.3$ |
| Stack | | 875.0 | $23.4\mathrm{e}{-}11 \pm 1.8$ | $1.89 \pm 0.06$ | 1300 | $12.5 \pm 1.6$ |

**Notes.** The epoch number is given in the first column and the corresponding date in the second. Other columns present the results of the analysis: TS, differential flux at the decorrelation energy, the spectral index $\Gamma$, the decorrelation energy, and integrated flux between 100 MeV and 500 GeV.

For completeness, the spectra averaged over the epochs 1, 3, 5, and 6 (Stereo mode observations) and over epochs 2 and 4 (Mono mode observations) were computed separately. Above 200 GeV, both measurements are compatible with each other, with an integrated flux of $(4.86 \pm 0.30) \times 10^{-6}$ ph cm$^{-2}$ s$^{-1}$ for the Stereo mode observations and $(2.59 \pm 0.38) \times 10^{-6}$ ph cm$^{-2}$ s$^{-1}$ for Mono mode observations. All the H.E.S.S. data were analysed together by combining the Stereo and Mono mode observations (see Holler et al. 2015), allowing us to compute an averaged spectrum (see Table 1). The integrated flux above 200 GeV measured for this combined analysis is $(3.12 \pm 0.47) \times 10^{-12}$ ph cm$^{-2}$ s$^{-1}$ TeV$^{-1}$. A cross check with a different analysis chain (Parsons & Hinton 2014) was performed and yields similar results.

## 2.2. Fermi-LAT data analysis and results

The *Fermi*-LAT is a $\gamma$-ray pair conversion telescope (Atwood et al. 2009) that is sensitive to $\gamma$-rays above 20 MeV. The bulk of LAT observations are performed in an all-sky survey mode ensuring a coverage of the full sky every 3 h.

Data and software used in this work (`Fermitools`) are publicly available from the Science Support Center[1]. Events within $10°$ around the radio coordinates of PKS 2155−304 (region of interest, ROI) and passing the `SOURCE` selection (Ackermann et al. 2012) were considered corresponding to event class 128 and event type 3 and a maximum zenith angle of $90°$. Further cuts on the energy ($100$ MeV $< E < 500$ GeV) were made, which remove the events with poor energy resolution. To ensure a significant detection of PKS 2155−304, time windows of 3 days centred on the campaign nights (Table 1) were considered to extract the spectral parameters. To analyse LAT data, `P8R3_SOURCE_V2` instrumental response functions (irfs) were used. In the fitting procedure, `FRONT` and `BACK` events (Atwood et al. 2009) were treated separately.

The Galactic and extragalactic background models designed for the `PASS 8` irfs denoted `gll_iem_v07.fits` (Acero et al. 2016) and `iso_P8R3_SOURCE_V2_v1.txt` were used in the sky model, which also contains all the sources of the fourth general *Fermi* catalogue (4FGL, The Fermi-LAT Collaboration 2020) within the ROI plus $2°$ to take into account the large point spread function (PSF) of the instrument especially at low energy.

An unbinned maximum likelihood analysis (Mattox et al. 1996) implemented in the `gtlike` tool[2] was used to find the best-fit spectral parameters of each epoch. Models other than the power-law reported here do not significantly improve the fit quality. Table 2 shows the results of the analysis. We note that for epoch 1 with a test statistic (TS) below 25 ($\approx 5\sigma$), a flux upper limit was derived assuming a spectral index of $\Gamma = 1.75$[3].

All the uncertainties presented in this section are statistical only. The most important source of systematic uncertainties in the LAT results is the uncertainty on the effective area, all other systematic effects are listed on the FSSC website[4].

## 2.3. NuSTAR data analysis and results

The *NuSTAR* satellite developed in the NASA Explorer program features two multilayer-coated telescopes that focus the reflected X-rays onto pixellated CdZnTe focal plane modules and provide an image of a point source with a half-power diameter of $\sim 1'$ (see Harrison et al. 2013, for more details). The advantage of *NuSTAR* over other X-ray missions is its broad bandpass, 3–79 keV with a spectral resolution of $\sim 1$ keV.

Table 3 provides the details of individual *NuSTAR* pointings: this includes the amount of on-source time (after screening for the South Atlantic Anomaly passages and Earth occultation) and mean net (background-subtracted) count rates. After processing the raw data with the *NuSTAR* Data Analysis Software (NuSTARDAS) package `v1.3.1` (with the script `nupipeline`), the source data were extracted from a region of $45''$ radius centred on the centroid of X-ray emission, while the background was extracted from a $1.5'$ radius region roughly $5'$ southwest of the source location located on the same chip. The choice of these parameters is dictated by the size of the point-spread function of the mirror. However, the derived spectra depend very weakly on the sizes of the extraction regions. The spectra were subsequently binned to have at least 30 total counts per re-binned channel. Spectral channels corresponding nominally to the 3–60 keV energy range were considered, in

---

[1] https://fermi.gsfc.nasa.gov/ssc/data

[2] An unbinned analysis is recommended for small time bins https://fermi.gsfc.nasa.gov/ssc/data/analysis/scitools/binned_likelihood_tutorial.html

[3] This value has been taken a priori and close to the index found in this work.

[4] https://fermi.gsfc.nasa.gov/ssc/data/analysis/LAT_caveats.html

**Table 3.** Summary of the *NuSTAR* observations of PKS 2155−304.

| Epoch | Start | Stop | Obs. ID | Exposure [ks] | Mod A ct rate | Mod B ct rate | Flux$_{2-10\mathrm{keV}}$ [$10^{-11}$ erg cm$^{-2}$ s$^{-1}$] | $\Gamma$ | $\chi^2$/PHA |
|---|---|---|---|---|---|---|---|---|---|
| 1 | 2013-07-16 22:51:07 | 2013-07-17 07:06:07 | 60002022004 | 13.9 | 0.245 | 0.235 | $1.43 \pm 0.07$ | $2.61 \pm 0.05$ | 248.3/269 |
| 2 | 2013-08-02 21:51:07 | 2013-08-03 06:51:07 | 60002022006 | 10.9 | 0.247 | 0.234 | $1.65 \pm 0.08$ | $3.09 \pm 0.05$ | 188.0/216 |
| 3 | 2013-08-08 22:01:07 | 2013-08-09 08:21:07 | 60002022008 | 13.4 | 0.149 | 0.133 | $0.90 \pm 0.05$ | $2.85 \pm 0.08$ | 153.8/159 |
| 4 | 2013-09-28 22:56:07 | 2013-09-29 06:26:07 | 60002022016 | 11.5 | 0.149 | 0.119 | $0.80 \pm 0.06$ | $2.73 \pm 0.07$ | 139.1/141 |
| 7 | 2013-08-14 21:51:07 | 2013-08-15 07:06:07 | 60002022010 | 10.5 | 0.229 | 0.213 | $1.44 \pm 0.06$ | $2.92 \pm 0.07$ | 188.8/195 |
| 8 | 2013-08-26 19:51:07 | 2013-08-27 03:06:07 | 60002022012 | 11.3 | 0.452 | 0.427 | $2.55 \pm 0.06$ | $2.64 \pm 0.04$ | 314.8/333 |
| 9 | 2013-09-04 21:56:07 | 2013-09-05 07:06:07 | 60002022014 | 12.2 | 0.251 | 0.228 | $1.46 \pm 0.06$ | $2.80 \pm 0.05$ | 208.8/238 |

**Notes.** The first columns are the epoch number, start and stop time of the observation, and the corresponding ID. The exposure, the count rate of each module, and the derived spectral parameters (integrated model flux and photon index) are given in subsequent columns. The last column is the $\chi^2$ over the number of bins (pulse height amplitude, PHA). For the power-law model, the number of degrees of freedom is two less than the number of PHA bins.
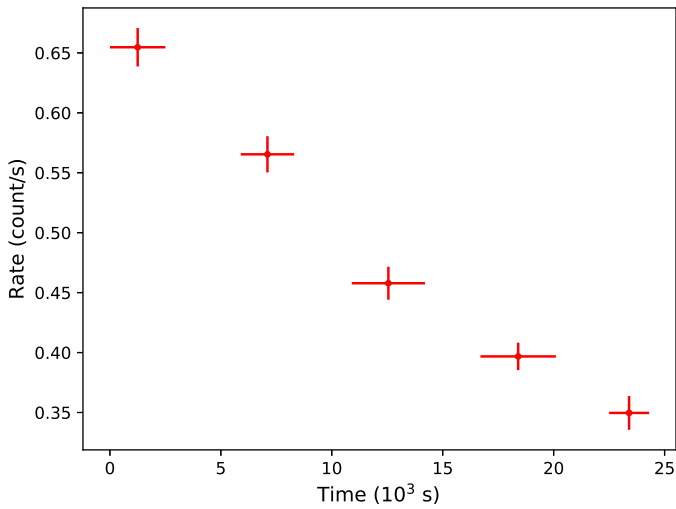


**Fig. 2.** Light curve of PKS 2155−304 as seen by the FPMA module of *NuSTAR* during the observation 60002022012 (epoch 8). The energy range is 3–60 keV and the plotted data are not background subtracted. However, the background rate is always lower than 0.03 counts per second and the background was steady (within 5%) throughout the observation. Each point corresponds to data taken over roughly one orbit, during the time indicated by the red markers.

which the source was robustly detected. The resulting spectral data were fitted with a power law modified by the Galactic absorption with a column density of $1.7 \times 10^{20}$ atoms cm$^{-2}$ (Dickey & Lockman 1990) using XSPEC v12.8.2. The standard instrumental response matrices and effective area were derived using the ftool nuproducts. The alternate $N_H$ measurement by Kalberla et al. (2005) of $1.4 \times 10^{20}$ cm$^{-2}$ was tested, and the best-fit spectral parameters of the source were entirely consistent with results obtained using Dickey & Lockman (1990) values. Data for both *NuSTAR* detectors were fitted simultaneously, allowing an offset of the normalisation factor for the focal plane module B (FPMB) with respect to module FPMA. Regardless of the adopted models, the normalisation offset was less than 5%. The resulting fit parameters are given in Table 3. More complex models for fitting to the datasets obtained during joint *NuSTAR* and *Swift*-XRT pointings were considered, and those are discussed in Sect. 3.2.

The source exhibited significant variability in one of the pointings on August 26 (epoch 8); the *NuSTAR* X-ray count rate for the FPMA module dropped by almost a factor of two in 25 ks

clock time (Fig. 2). This was observed independently by both *NuSTAR* modules. The other *NuSTAR* observations showed only modest variability, with a nominal min-to-max amplitude of less than 20% of the mean count rate. Such variability is not uncommon in HBL-type BL Lac objects and has been seen in previous observations of PKS 2155−304 (see, e.g. Zhang 2008). More recently, rapid X-ray variability was seen in PKS 2155−304 when it was simultaneously observed by many X-ray instruments (Madsen et al. 2017). Other HBL-type blazars exhibit similar variability; recent examples are Mkn 421 (Baloković et al. 2016) and Mkn 501 (Furniss et al. 2015).

### 2.4. Swift-XRT data analysis and results

The details of the *Swift* X-ray Telescope (XRT, Burrows et al. 2005) observations used here are listed in Table 4. The observations were taken simultaneously (or as close as possible) with the H.E.S.S. and *NuSTAR* observations. During this campaign, *Swift* observed the source nine times, but for one of the pointings (corresponding to epoch 6, archive sequence 00030795110), applying standard data quality cuts resulted in no useful source data (the source was outside of the nominal Window Timing – WT – window). Two *Swift*-XRT observations (sequences 0080280006 and -08) were close in time and were performed during a single *NuSTAR* observation. Because these observations have consistent fluxes and spectra, they were added together as *Swift*-XRT data for epoch 7.

All *Swift*-XRT observations were carried out using the WT readout mode. The data were processed with the XRTDAS software package (version 3.4.0) developed at Space Science Data Center (SSDC[5]) and distributed by HEASARC within the HEASoft package (version 6.22.1). Event files were calibrated and cleaned with standard filtering criteria with the xrtpipeline task using the calibration files available in the *Swift* CALDB (v. 20171113). The average spectrum was extracted from the summed and cleaned event file. Events for the spectral analysis were selected within a circle of 20 pixels (~46″) radius, which encloses about 80% of the PSF, centred on the source position. The background was extracted from a nearby circular region of 20 pixels radius. The ancillary response files (ARFs) were generated with the xrtmkarf task applying corrections for PSF losses and CCD defects using the cumulative exposure map. The latest response matrices (version 15) available in the *Swift* CALDB were used. Before the spectral fitting, the 0.4–10 keV

---

[5] https://swift.asdc.asi.it/

source spectra were binned to ensure a minimum of 30 counts per bin. The data extending to the last bin with 30 counts were used, which is typically ∼5 keV.

The spectrum of each *Swift*-XRT observation was fitted with a simple power law with a Galactic absorption column of $1.7 \times 10^{20}$ atoms cm$^{-2}$ using the XSPEC v12.8.2 package. The resulting mean count rates, power law indices, and corresponding 2–10 keV model fluxes are also included in Table 4. No variability was found in individual observations in this energy range.

### 2.5. Spectral fitting of X-ray data and the search for the hard X-ray "tail"

The results of the individual spectral fits of the *Swift*-XRT and *NuSTAR* data are given in Tables 3 and 4, respectively. However, because PKS 2155−304 exhibited complex X-ray spectral structure measured in the joint *XMM-Newton* plus *NuSTAR* observation in April 2013 (Madejski et al. 2016), here a joint fit to the lower-energy *Swift*-XRT and the higher-energy *NuSTAR* data was performed to investigate the need for such increasingly complex models. Since the source is highly variable, only the strictly simultaneous *Swift*-XRT and *NuSTAR* data sets were paired. To account for possible effects associated with variability or imperfect *Swift*-XRT-to-*NuSTAR* cross-calibration, the normalisations of the models for the two detectors were allowed to vary, but the difference was in no case greater than 20%, consistent with the findings of Madsen et al. (2017), with the exception of the August 26 observation (epoch 8) where *NuSTAR* revealed significant variability (see note in Sect. 2.3).

To explore the spectral complexity similar to that seen in April 2013, the following models were considered[6]: (1) PL: a simple power-law model; and (2) LP: a log-parabola model. The resulting joint spectral fits are given in Table 5.

In four observations (epochs 1, 3, 4 and 9), the model consisting of a simple PL absorbed by the Galactic column fits the data well: no deviation from a simple power-law model is required. However, for epochs 2, 7, and 8, a significant improvement ($\Delta\chi^2 > 20$ for one extra parameter) of the fit quality is found by adopting the LP model. Thus, at these epochs, the spectrum steepens with energy. In conclusion, there are not only *spectral index* changes from one observation epoch to another, but there is also a significant change of the spectral curvature from one observation to another. Bhatta et al. (2018), using only *NuSTAR* data, reported results on the same observations and also found a change in the spectral shape for epoch 8 but not for epochs 2 or 7. These latter authors also reported a hardening for epochs 1, 3, and 4, but one which is not significant when compared to a PL fit.

A third model consisting of one log-parabola plus a second hard power law with spectral index $\Gamma_{HT}$ (LPHT)[7] was also tested. The model adds a generally harder high-energy "tail" (HT) to the softer log-parabola component. A notable feature is the absence of such a HT in any of the observations (see Sect. 3.2). Therefore, an upper limit on the 20–40 keV flux was computed assuming $\Gamma_{HT} = 2$.

### 2.6. Swift-UVOT data analysis and results

The Ultraviolet/Optical Telescope (UVOT; Burrows et al. 2005) on board *Swift* also observed PKS 2155−304 during *Swift* pointings and measured the UV and optical emission in the bands *V*

(500–600 nm), *B* (380–500 nm), *U* (300–400 nm), *UVW1* (220–400 nm), *UVM2* (200–280 nm) and *UVW2* (180–260 nm). The values of Schlafly & Finkbeiner (2011) were used to correct for the Galactic absorption[8].

The photon count-to-flux conversion is based on the UVOT calibration (Sect. 11 of Poole et al. 2008). A power-law spectral index $\Gamma_{UV}$ was derived for each epoch and is reported in Table 6. The results presented in this work do not provide evidence for spectral variability in the UV energy range.

## 3. Discussion

### 3.1. Flux state and variability in γ-rays

During the observation campaign, PKS 2155−304 was found in a low flux state, in the H.E.S.S. energy range, $\phi(E > 200\text{GeV}) = (11.6 \pm 1.3) \times 10^{-12}$ ph cm$^{-2}$ s$^{-1}$, a factor of approximately five lower than during the 2008 campaign ($\phi(E > 200\text{GeV}) = (57.6 \pm 1.8) \times 10^{-12}$ ph cm$^{-2}$ s$^{-1}$ Aharonian et al. 2009); see Fig. 3. The average flux above 200 GeV measured by H.E.S.S. during 9 years of observations ($\phi(E > 200\text{GeV}) = (51.0 \pm 4.1) \times 10^{-12}$ ph cm$^{-2}$ s$^{-1}$, H.E.S.S. Collaboration 2017a) is also more than four times higher than that reported here (for the entire campaign). We note that even lower flux values have been measured over the last 10 years (see Fig. 1 of H.E.S.S. Collaboration 2017a). The source exhibits a harder spectrum ($\Gamma \approx 2.8$) with respect to the H.E.S.S. phase I measurement ($\Gamma \approx 3.4$, Aharonian et al. 2009; H.E.S.S. Collaboration 2017a). This is consistent with the results of H.E.S.S. Collaboration (2017b) and likely to be due to the lower energy threshold achieved with CT5.

The *Fermi*-LAT flux averaged over the nine epochs was lower than the flux measured in the 3FGL, $(12.6 \pm 0.4) \times 10^{-8}$ ph cm$^{-2}$ s$^{-1}$, and lower than in 2008 by a factor of approximately two. Similar results were found by H.E.S.S. Collaboration (2017b) showing that the source was in a low flux state in 2013. With a flux of $(8 \pm 2) \times 10^{-8}$ ph cm$^{-2}$ s$^{-1}$ in the 100 MeV–300 GeV energy range, epoch 0 is not different from the epochs reported here. The 2−10 keV X-ray flux was found to be a factor of between approximately three and four lower than in 2008 (Aharonian et al. 2009); see Fig. 3. Only at two epochs (3 and 4), was the 2−10 keV flux measured by *NuSTAR* lower than the one measured at epoch 0 ($1.1 \times 10^{-11}$ erg cm$^{-2}$ s$^{-1}$) and the fluxes of epochs 1, 2, 7, 8, and 9 were higher. The only noticeable difference is at lower energies with the observed optical flux measured by *Swift*-UVOT: at epoch 0, the flux was higher than that measured in all the other epochs (see Table 6).

### 3.2. Broad-band X-ray spectrum

In the energy range from 0.3 to 10 keV, the spectrum is usually assumed to be the high-energy end of the synchrotron emission. Indeed, the measured spectral index of PKS 2155−304 in the X-ray regime is generally in agreement with the value expected for a HBL, for which a power-law spectral index, $\Gamma$, is typically steeper than 2 ("soft component" hereafter). Nevertheless a single power law is too simple a representation of the spectrum when measured with sensitive instruments affording a good signal-to-noise ratio. As already pointed out by Perlman et al. (2005), the soft X-ray spectra of HBLs are well represented

---

[6] Models are corrected for Galactic absorption.
[7] The formula for this LPHT model is $\phi \propto E^{-\Gamma-\beta\cdot\log(E)} + E^{-\Gamma_{HT}}$.

[8] See https://irsa.ipac.caltech.edu/applications/DUST/index.html with a reddening ratio $A_v/E(B-V) = 3.1$ and $E(B-V) = 0.022$.

**Table 4.** Summary of the *Swift*-XRT observations of PKS 2155−304.

| Epoch | Start | Stop | Obs. ID | Exposure [ks] | Ct. rate [cts s$^{-1}$] | Flux$_{2-10\mathrm{keV}}$ [$10^{-11}$ erg cm$^{-2}$ s$^{-1}$] | $\Gamma$ | $\chi^2$/PHA |
|---|---|---|---|---|---|---|---|---|
| 1 | 2013-07-17 00:06:58 | 2013-07-17 02:41:34 | 00080280001 | 1.6 | 1.67 | 1.7 ± 0.1 | 2.43 ± 0.06 | 79.0/77 |
| 2 | 2013-08-03 00:20:59 | 2013-08-03 02:50:45 | 00080280002 | 2.1 | 2.56 | 1.9 ± 0.1 | 2.63 ± 0.05 | 118.2/124 |
| 3 | 2013-08-08 23:06:59 | 2013-08-09 00:21:47 | 00080280003 | 1.7 | 1.36 | 1.0 ± 0.1 | 2.71 ± 0.07 | 64.8/65 |
| 4 | 2013-09-28 22:50:59 | 2013-09-29 00:06:47 | 00080280015 | 1.6 | 1.07 | 0.8 ± 0.1 | 2.69 ± 0.08 | 40.8/53 |
| 5 | 2013-06-05 19:37:59 | 2013-06-05 20:43:12 | 00030795109 | 0.9 | 1.61 | 1.4 ± 0.2 | 2.57 ± 0.09 | 45.4/45 |
| 7 | 2013-08-14 23:15:45 | 2013-08-15 02:13:48 | 00080280006 and −08 | 1.8 | 2.32 | 2.0 ± 0.1 | 2.59 ± 0.05 | 89.2/108 |
| 8 | 2013-08-26 20:17:59 | 2013-08-26 23:06:38 | 00080280009 | 1.0 | 3.1 | 3.4 ± 0.2 | 2.38 ± 0.06 | 68.1/85 |
| 9 | 2013-09-05 04:33:59 | 2013-09-05 05:39:41 | 00080280013 | 0.9 | 0.85 | 1.5 ± 0.2 | 2.65 ± 0.10 | 17.2/28 |

**Notes.** The first columns are the epoch number, the start and stop time of the observation, and the corresponding ID. The observation length, the count rate, and the derived spectral parameters (integrated model flux and photon index) are given in subsequent columns. The last column is the $\chi^2$ over the number of PHA bins (PHA). For the power-law model, the number of degrees of freedom is two less than the number of PHA bins.

**Table 5.** Joint *NuSTAR* and *Swift*-XRT observations of PKS 2155−304.

| Epochs | PL index $\Gamma$ | $\chi^2_{\mathrm{PL}}$/PHA | LP index $\Gamma$ [a] | LP curvature $\beta$ | $\chi^2_{\mathrm{LP}}$/PHA | Flux$_{\mathrm{HT}}$(20−40 keV) [b] [$10^{-12}$ erg cm$^{-2}$ s$^{-1}$] |
|---|---|---|---|---|---|---|
| 1 | 2.54 ± 0.04 | 341.3/346 | $2.57^{+0.13}_{-0.03}$ | 0.13 ± 0.06 | 332.1/346 | <1.2 |
| 2 | 2.80 ± 0.03 | 414.0/340 | $3.01^{+0.12}_{-0.04}$ | 0.27 ± 0.07 | 301.7/340 | <0.4 |
| 3 | 2.77 ± 0.05 | 223.5/224 | 2.82 ± 0.07 | 0.09 ± 0.06 | 218.9/224 | <0.8 |
| 4 | 2.71 ± 0.06 | 179.5/194 | 2.71 ± 0.06 | 0.00 ± 0.07 | 179.5/194 | <0.8 |
| 7 | 2.72 ± 0.04 | 327.8/303 | $2.86^{+0.11}_{-0.05}$ | $0.18^{+0.08}_{-0.04}$ | 281.6/303 | <0.5 |
| 8 | 2.56 ± 0.03 | 425.1/418 | 2.59 ± 0.03 | 0.17 ± 0.04 | 378.2/418 | <0.8 |
| 9 | 2.78 ± 0.05 | 229.5/266 | 2.78 ± 0.05 | 0.10 ± 0.15 | 226.7/266 | <1.3 |

**Notes.** The errors quoted on the spectral parameters as well as the quoted 20–40 keV flux limits are 90% level confidence regions. For the log-parabola model, the number of degrees of freedom is four less than the number of PHA bins, since the LP model has one extra parameter, and in addition, the normalisation of the two instruments is fitted separately. The 2–10 keV flux for joint *Swift* and *NuSTAR* spectral fits is essentially the same as that measured by *NuSTAR* alone. [a]$\Gamma$ is evaluated at 5 keV. [b]The hard tail index is assumed to have $\Gamma_{\mathrm{HT}}$ of 2.

**Table 6.** *Swift*-UVOT observations of PKS 2155−304.

| Epochs | V 2.30 eV | B 2.86 eV | U 3.54 eV | UVW1 4.72 eV | UVM2 5.57 eV | UVW2 6.12 eV | $\Gamma_{\mathrm{UV}}$ |
|---|---|---|---|---|---|---|---|
| 0 [*] | 71 ± 2 | 73 ± 2 | 78 ± 3 | 75 ± 3 | 88 ± 3 | 81 ± 3 | |
| 1 | 54.2 ± 1.5 | 56.0 ± 1.2 | 59.6 ± 1.4 | 59.4 ± 1.2 | 67.1 ± 1.4 | 60.1 ± 1.1 | 1.86 ± 0.14 |
| 2 | 59.9 ± 1.6 | 65.4 ± 1.4 | 66.5 ± 1.5 | 69.5 ± 1.4 | 79.5 ± 1.6 | 71.1 ± 1.3 | 1.80 ± 0.14 |
| 3 | 49.8 ± 1.3 | 54.4 ± 1.1 | 51.5 ± 1.2 | 57.8 ± 1.1 | 64.9 ± 1.3 | 62.1 ± 1.1 | 1.77 ± 0.14 |
| 4 | 57.0 ± 1.4 | 60.5 ± 1.2 | 61.4 ± 1.4 | 62.9 ± 1.2 | 72.3 ± 1.4 | 63.1 ± 1.1 | 1.86 ± 0.14 |
| 5 | 53.7 ± 1.6 | 58.5 ± 1.4 | 65.3 ± 1.6 | 64.7 ± 1.4 | 75.8 ± 1.6 | 65.7 ± 1.2 | 1.76 ± 0.14 |
| 7 | 62.1 ± 1.8 | 64.3 ± 1.5 | 73.3 ± 1.8 | 74.3 ± 1.5 | 84.5 ± 1.9 | 74.6 ± 1.4 | 1.76 ± 0.14 |
| 8 | 59.1 ± 1.8 | 60.7 ± 1.5 | 65.6 ± 1.6 | 70.1 ± 1.5 | 79.4 ± 1.7 | 70.1 ± 1.3 | 1.76 ± 0.14 |
| 9 | 62.5 ± 1.8 | 68.6 ± 1.6 | 68.0 ± 1.6 | 70.6 ± 1.5 | 81.4 ± 1.7 | 72.6 ± 1.4 | 1.83 ± 0.14 |

**Notes.** The fluxes are given in units of $10^{-12}$ erg cm$^{-2}$ s$^{-1}$. The last column is the power-law spectral index $\Gamma_{\mathrm{UV}}$ obtained by fitting the UVOT data. [*]Values taken from Madejski et al. (2016).

as gradually steepening functions towards higher energies. In the data presented here, the spectral index measured by *Swift*-XRT is always harder than the one measured by *NuSTAR*. A Kolmogorov–Smirnov test was performed on both *Swift*-XRT and *NuSTAR* spectral index distributions. This test rejects the hypothesis that they are sampled from the same distribution with a *p*-value of 3%. This suggests that such steepening takes place for PKS 2155−304.

At the end of the X-ray spectrum (roughly above a few keV), Urry & Mushotzky (1982) observed PKS 2155−304 above an energy of a few keV with the HEAO A1 instrument, and Zhang (2008) reported a hard excess in two *XMM-Newton* observations (confirmed by Foschini et al. 2008 using the same observations). The *XMM-Newton* observations fit with a broken power-law showed a spectral hardening of $\Delta\Gamma = 0.1-0.3$ with a break energy of 3–5 keV. Both works interpreted this as a possible
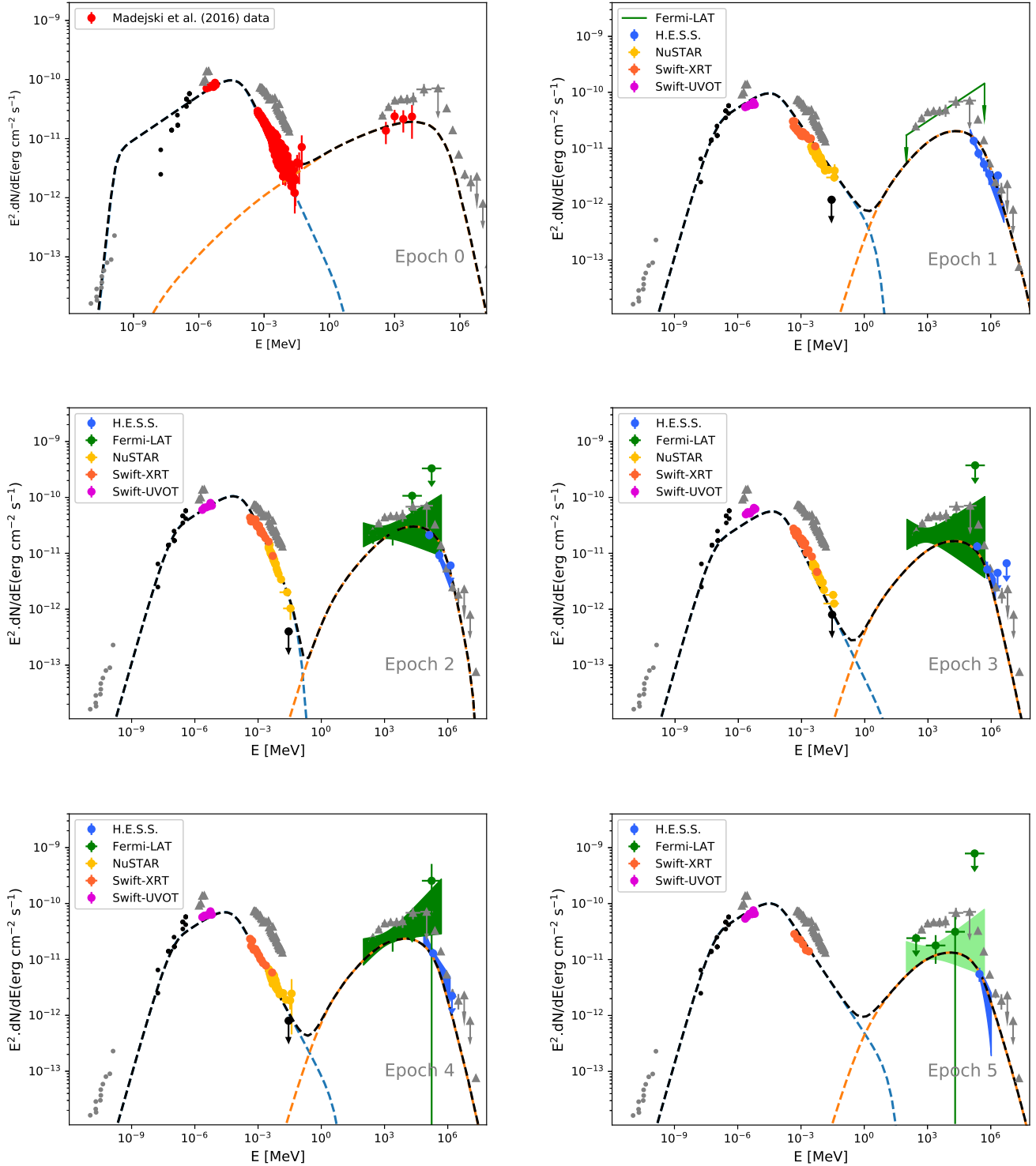
**Fig. 3.** Spectral energy distribution of PKS 2155−304 for each epoch considered in this work. For epoch 0, the red points are directly extracted from Madejski et al. (2016). In the other plots, the purple points are UVOT data, orange are XRT data, and yellow are the *NuSTAR* data. In γ-rays, the green points and contours are the *Fermi*-LAT results and H.E.S.S. results are in blue. The black upper limits refer to the hard-tail component (see text) and are used to constrain the inverse-Compton part of the SSC model (black line). The grey points are the data from the 2008 observation campaign (Aharonian et al. 2009) shown for comparison. Black points are the radio data from Abdo et al. (2010) and Liuzzo et al. (2013). The dashed blue line is the synchrotron emission and the orange line is the IC emission. Both are from the SSC calculation, and the black dashed line is the sum of both.

contamination of the synchrotron spectra by inverse-Compton emission.

More recently, and with the increased energy range provided by *NuSTAR*, Madejski et al. (2016) also measured a hard tail in

the X-ray spectrum of PKS 2155−304 (April 2013 observations, epoch 0). Using a broken power-law model, they found a flattening spectrum with a spectral break of $\Delta\Gamma > 1$ around 10 keV. During that observation, the source was found in a very low flux

state (with the 2–10 keV flux of $1.1 \times 10^{-11}$ erg cm$^{-2}$ s$^{-1}$), even lower than the flux reported by Zhang (2008) and Foschini et al. (2008). Jointly fitting the strictly simultaneous *XMM-Newton* data with the *NuSTAR* data, a more complete picture emerged, with a log-parabola describing the soft ($E < 5$ keV) spectrum, and a hard tail which can be described as an additional power law.

Regarding the observations presented in this work, adding an extra hard tail (LPHT model) does not significantly improve the $\chi^2$. However, it is important to note that the flux of the object during the April 2013 pointing was relatively low, and the observations were fairly long (about four times longer than any single pointing during the campaign reported here). As noted by Madejski et al. (2016), the hard tail becomes more easily detectable only during low-flux states of the softer, low-energy spectral component.

To detect a possible hard tail in the data set of the present campaign, a simultaneous spectral fit of all data sets was performed. Due to the spectral variability of the soft, low-energy component (Table 3), stacking (or just summing) all spectra simultaneously is inappropriate. Instead, a simultaneous fit of seven individual datasets from Epochs 1, 2, 3, 4, 7, 8, and 9 was considered, allowing the spectral parameters of the soft component (described as a log-parabola) to vary independently. Each epoch was described by a LPHT model (see Sect. 2.5), and with common normalisation of the hard tail for all data sets[9]. Formally, the fit returns zero flux for the hard-tail component. The 99% confidence upper limit of $1.8 \times 10^{-4}$ ph keV$^{-1}$ cm$^{-2}$ on the normalisation of this component (at $\chi^2 + 2.7$) corresponds to a 20–40 keV flux limit of $2.5 \times 10^{-13}$ erg cm$^{-2}$ s$^{-1}$. The normalisation of this hard tail in the data from epoch 0 is $8 \times 10^{-4}$ ph keV$^{-1}$ cm$^{-2}$ (corresponding to a 20–40 keV flux of $12.0 \times 10^{-13}$ erg cm$^{-2}$ s$^{-1}$), or more than four times higher than the upper limit measured during the other epochs. In conclusion, the hard tail is also variable on a timescale of months, but no conclusions on the shorter timescales from the presented *NuSTAR* data can be drawn.

We note that the source does exhibit a similar flux level in X-rays with respect to the April 2013 data set while in optical, the flux is significantly lower. In an SSC framework, this photon field might be scattered by low-energy electrons to produce hard X-ray photons accounting for the hard tail visible in epoch 0. Nevertheless, when the *Fermi* measurement is extrapolated down towards the *NuSTAR* energy range, it always overshoots the X-ray measurement. This could be due to a lack of statistics in the LAT range preventing the detection of spectral curvature such as that reported in the 3FGL catalogue, since only 3 days of data were used in each epoch. The extrapolation of the 3FGL spectrum of PKS 2155−304 does not violate the upper limits derived here on the hard-tail component but cannot reproduce epoch 0.

## 4. SED modelling

### 4.1. Leptonic modelling: one zone synchrotron self-Compton

Modelling of blazar SEDs was performed with a one-zone SSC model by Band & Grindlay (1985). The emission zone is considered to be a sphere of radius $R$ filled with a magnetic field $B$ and moving at relativistic speed with a Lorentz factor $\Gamma$. In this zone, the emitting particle distribution follows a broken power

law:

$$n_e(\gamma) = \begin{cases} N\gamma^{-p_1} & \text{if } \gamma_{\min} < \gamma < \gamma_b, \\ N\gamma^{-p_2}\,\gamma_b^{p_2-p_1} & \text{if } \gamma_b < \gamma < \gamma_{\max}, \end{cases} \quad (1)$$

where $N$ is density of electrons at $\gamma = 1$, $p_1$ and $p_2$ are the indices of the electron distribution, and $\gamma_b$ is the break energy.

The modelling was performed on the epochs presented in this work (1–5) with UV, X-ray, GeV, and TeV data. Radio data from Abdo et al. (2010) and Liuzzo et al. (2013) were taken from the NED[10]. The radio emission could originate from another location in the jet, or from the emission zone, and is therefore considered as an upper limit in the model. Historical data taken between $10^{-2}$ eV and 1 eV (infra-red range) are found to be quite stable in time with variation of less than a factor of two. Such data were collected using Vizier[11] and shown in the SEDs.

For each epoch, a mathematical minimisation (Nelder & Mead 1965) was performed to find the model parameters $R$, $B$, $N$, $\log(\gamma_{\min})$, $\log(\gamma_b)$, and $\log(\gamma_{\max})$ that best fit the data. The values of $p_1$ and $p_2$ were constrained by the UV and X-ray data, respectively, and were not allowed to vary freely in the fitting procedure. Given the little spectral variability found in UV and GeV, $p_1$ was set to 2.5 and $p_2 = 2\cdot\Gamma_{\text{X-ray}}-1$ (Rybicki & Lightman 1986). The minimisation was performed using a Markov chain Monte Carlo (MCMC) implemented in the `emcee` python package (Foreman-Mackey et al. 2013). For epochs 1–4, the upper limit on the hard-tail flux (Table 5) is taken into account by forcing the inverse-Compton (IC) component of the model to be below this limit. The resulting parameters are given in Table 7 with their corresponding realisations in Fig. 3.

The model parameters are consistent with previous studies by Kataoka et al. (2000), Foschini et al. (2007), Katarzynski et al. (2008), and Aharonian et al. (2009). As in these previous studies, as well as for other BL Lac objects (e.g. Mrk 421 (Abdo et al. 2011a), Mrk 501 (Abdo et al. 2011b), SHBL J001355.9–185406 (H.E.S.S. Collaboration 2013), etc.), the obtained model is far from equipartition. Even with a very low flux state in the present modelling, particles carry at least ten times more energy density than the magnetic field.

The data from epochs 1–5 are well reproduced by the simple SSC calculation presented here. In contrast to Gaur et al. (2017) for this object or Chen (2017) for Mrk 421, there is no need to invoke a second component to reproduce the SED without over-predicting the radio flux. The main difference is that the hard tail above $\approx 10$ keV seen in the previous observations is not observed in the present data set.

The SSC model was applied to the data of epoch 0 and results are also presented in Table 7. The contemporaneous data are well reproduced. The main difference in the modelling parameters between epoch 0 and the campaign presented in this work lies in the values of $\gamma_{\min}$. For epoch 0, having $\log(\gamma_{\min}) = 0$ allows a greater inverse-Compton contribution in the X-ray band, making the X-ray tail detectable by *NuSTAR*. This is also in agreement with the observed decrease in the optical flux in epochs 1–5. Indeed a higher value of $\gamma_{\min}$ decreases the number of electrons emitting in this energy range. We also note that the archival radio data are in disagreement with the modelling of epoch 0, which predict an overly high flux in that energy range. The values obtained for different parameters are not equally well constrained. The shape of the electron distribution ($\gamma_{\min}$, $\gamma_{\text{break}}$ and

---

[9] In an SSC or lepto-hadronic scenario, one would expect the hard X-ray tail to be the low-energy counterpart of the *Fermi* spectra. The approach made here with the assumption of a constant normalisation for the tail is more conservative than using the $\gamma$-ray spectral results.

[10] http://ned.ipac.caltech.edu/
[11] http://cds.u-strasbg.fr/vizier-org/licences_vizier.html

**Table 7.** Model parameters for each epoch.

| Epoch | $\log(\gamma_{\min})$ | $\log(\gamma_{\rm b})$ | $\log(\gamma_{\max})$ | $p_1$ | $p_2$ | $\delta$ | $B$ [$10^{-2}$ G] | $R$ [$10^{16}$ cm] | $N_{\rm tot}$ [$10^{+50}$] | $U_{\rm e}/U_{\rm b}$ |
|---|---|---|---|---|---|---|---|---|---|---|
| 0 | $0.21^{+0.01}_{-0.01}$ | $4.69^{+0.01}_{-0.01}$ | $7.09^{+0.11}_{-0.20}$ | 2.5 | 4.60 | $33.0^{+1.8}_{-1.7}$ | $4.2^{+0.2}_{-0.3}$ | $5.9^{+0.6}_{-0.5}$ | $4317.8^{+322.9}_{-617.9}$ | 722.0 |
| 1 | $3.55^{+0.06}_{-0.11}$ | $4.96^{+0.06}_{-0.08}$ | $7.31^{+0.43}_{-0.54}$ | 2.5 | 4.10 | $27.1^{+1.7}_{-1.5}$ | $1.2^{+0.4}_{-0.3}$ | $24.5^{+16.0}_{-7.7}$ | $5.8^{+2.6}_{-2.2}$ | 11.8 |
| 2 | $3.39^{+0.06}_{-0.07}$ | $5.02^{+0.04}_{-0.07}$ | $6.27^{+0.21}_{-0.19}$ | 2.5 | 4.60 | $32.4^{+2.0}_{-1.5}$ | $2.0^{+0.3}_{-0.3}$ | $10.6^{+2.3}_{-5.1}$ | $2.7^{+937.2}_{-0.8}$ | 18.7 |
| 3 | $3.39^{+0.10}_{-0.16}$ | $4.95^{+0.11}_{-0.09}$ | $7.55^{+0.17}_{-0.57}$ | 2.5 | 4.54 | $29.2^{+3.2}_{-4.1}$ | $1.7^{+1.2}_{-0.7}$ | $10.8^{+5.1}_{-6.5}$ | $2.9^{+1.5}_{-2.9}$ | 23.4 |
| 4 | $3.32^{+0.11}_{-0.10}$ | $4.73^{+0.11}_{-0.11}$ | $7.14^{+0.47}_{-0.53}$ | 2.5 | 4.42 | $30.6^{+4.0}_{-2.3}$ | $3.1^{+1.4}_{-1.2}$ | $6.2^{+5.7}_{-2.9}$ | $1.6^{+1.5}_{-0.7}$ | 19.1 |
| 5 | $3.29^{+0.10}_{-0.14}$ | $4.74^{+0.08}_{-0.15}$ | $7.42^{+0.43}_{-1.04}$ | 2.5 | 4.14 | $32.8^{+2.2}_{-3.4}$ | $2.8^{+2.9}_{-0.8}$ | $7.4^{+0.4}_{-1.0}$ | $1.6^{+1.0}_{-0.9}$ | 5.6 |

**Notes.** Errors were estimated from the MCMC distributions. The first column recalls the epoch, followed by minimal, break, and maximal energies, and the indices $p_1$ and $p_2$. The last parameters are the $B$-field, size of the region $R$, and the total number of electrons $N_{\rm tot}$. The equipartition factor (ratio of the energy carried by electron over energy in the magnetic field $U_{\rm e}/U_{\rm b}$) is given in the last column.
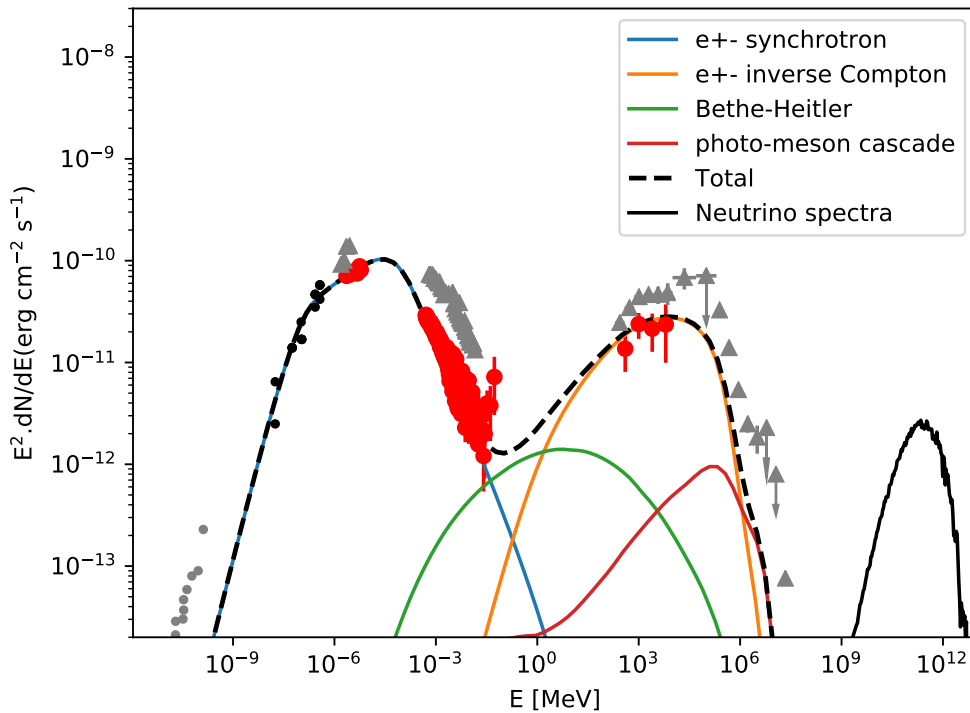


**Fig. 4.** Same as Fig. 3 but for epoch 0 only. The blue and orange dashed lines are the synchrotron and inverse-Compton emission as in Fig. 3. The green line is the emission from Bethe–Heitler pair-production and the red line is that from the photo-meson cascade. The sum of all these components is given by the black dashed line. The black continuous line is the predicted neutrino spectrum.

$\gamma_{\max}$) is quite robust with small errors. Other parameters like the $B$-field or the size of the emitting region remain poorly known and are indeed different from the model presented in Madejski et al. (2016).

### 4.2. Emergence of a hadronic component in hard X-rays?

Following the detection of a $\gamma$-ray flare from TXS 0506+056 coinciding with a high-energy neutrino (IceCube Collaboration 2018), several authors have independently shown that, while pure hadronic models cannot reproduce the multi-messenger dataset, a scenario in which the photon emission is dominated by an SSC component with a subdominant hadronic component is viable (see, e.g. Ansoldi et al. 2018; Cerruti et al. 2018; Gao et al. 2019; Keivani et al. 2018). The hadronic component emerges in the hard-X-rays as synchrotron radiation by secondary leptons produced via the Bethe–Heitler pair-production channel in this scenario. With this result in mind, it was investigated whether the hardening seen in the *NuSTAR* data of PKS 2155−304 could be

due to subdominant hadronic emission. Starting from the simple SSC model for epoch 0 (see Table 7), a population of relativistic protons was added. It was assumed that $p_{\rm p} = p_{\rm e,1}$ (i.e. protons and electrons share the same acceleration mechanism, resulting in the same injection spectral index) and that the maximum proton Lorentz factor $\gamma_{\rm p,max}$ is determined by equating acceleration and cooling timescales. The proton distribution was normalised such that the hadronic component emerges in hard X-rays. For additional details on the hadronic code used see Cerruti et al. (2015). Another change in the SSC part of the model was the increase of the value of $\log(\gamma_{\min})$ to 3.3 in order to avoid over-shooting the radio emission.

The key parameter is the power in protons $L_{\rm p}$ required to provide the observed photon flux, because a very well-known drawback of hadronic blazar models is that they often require proton powers well above the Eddington luminosity $L_{\rm Edd}$ of the super-massive black hole which powers the AGN. For the case of PKS 2155−304, if $p_{\rm p} = 2.5$, $\gamma_{\rm p,min} = 1$ and $\log \gamma_{\rm p,max} = 8.0$, then $L_{\rm p} = 5.6 \times 10^{50}$ erg s$^{-1}$ is needed, which is around $1000 L_{\rm Edd}$

for a black hole mass of $10^9_{M_\odot}$, making this scenario unrealistic. This result is very sensitive to the exact shape of the proton distribution, especially at low Lorentz factors (which cannot be constrained by the data). Moreover, $L_p$ is lower if the proton distribution is harder, or if $\gamma_{p,min} > 1$. As an example, if $p_p = 2.0$ and $\gamma_{p,min} = 1000$, then $L_p = 6.6 \times 10^{47}$ erg s$^{-1}$, which is of the same order of magnitude as $L_{Edd}$. For this scenario, the hadronic photon emission is shown in Fig. 4, and emerges in X-rays as the emission by Bethe–Heitler pairs, and at VHE as a photo-meson cascade. The model predicts an expected neutrino rate in IceCube of $\nu_{rate} = 0.01$ yr$^{-1}$, which is compatible with the non-detection of PKS 2155−304 by IceCube (computed using the IC effective area[12] for a declination of −30°).

## 5. Conclusions

PKS 2155−304 was observed contemporaneously for the first time by *Swift*, *NuSTAR*, *Fermi*-LAT, and H.E.S.S. The source was found in a low flux state in all wavelengths during epochs 1–9. The source flux is lower than during the campaign carried out in 2008.

For each epoch, no hard tail was detected in the X-ray spectra, contrary to what was seen at epoch 0. The computation of an upper limit on the 20–40 keV flux of such a hard tail for each observation and for the full data set shows that this component is variable on a timescale of a few months. For epochs 1–5, the SED is well reproduced by a one-zone SSC model. Such a model fails to reproduce the epoch 0 data due to the required value of the $\gamma_{min}$ parameter. A low value of $\gamma_{min}$ is mandatory to reproduce the hardening in X-rays but in return produces an overly high flux in the radio band with respect to the archival measurements.

The emergence of the variable X-ray hard tail cannot be explained by a one-zone SSC model. Several authors have proposed a multi-zone model to tackle this issue, and Gaur et al. (2017) in particular used a spine or layer jet structure. In such a structured jet, synchrotron photons of the slow layer are Comptonised by the electrons of the fast spine to produce the hard X-ray tail. The results presented here would imply that the layer producing the hard tail is variable over a timescale of months. Such a result is in agreement with the model parameters of Gaur et al. (2017). Nevertheless, the variability timescale derived from the model parameters of these latter authors cannot reproduce variability of the source on a timescale of days, as the model was not designed to reproduce such variability.

Here, the possibility of having a lepto-hadronic radiation component was explored. The same parameters as for the SSC model but with $\log(\gamma_{min}) = 3.3$ were used to reproduce a large part of the SED. The hard tail was successfully reproduced by the hadronic emission. Nevertheless for such a model to be in agreement with the Eddington luminosity of the super-massive black hole, the proton distribution has to be harder ($p_e = 2.0$) than the electron distribution ($p_e = 2.3$) together with $\gamma_{p,min} > 1000$ and/or have a low-energy cut-off $\gamma_{p,min} > 1$. In the framework of the lepto-hadronic model, the hard-X-ray emission associated with Bethe–Heitler pair production is independent and is not directly associated with the electron-synchrotron and the SSC components. The detection of the hard-X-ray tail during only one of the *NuSTAR* observations could therefore be explained by a sudden increase in the hadronic injection. The origin of the hard tail is still uncertain but this feature could help to disentangle different classes of emission models for PKS 2155−304 and blazars in general.

## References

Abdo, A. A., Ackermann, M., Agudo, I., et al. 2010, ApJ, 716, 30
Abdo, A. A., Ackermann, M., Ajello, M., et al. 2011a, ApJ, 736, 131
Abdo, A. A., Ackermann, M., Ajello, M., et al. 2011b, ApJ, 727, 129
Acero, F., Ackermann, M., Ajello, M., et al. 2015, ApJS, 218, 23
Acero, F., Ackermann, M., Ajello, M., et al. 2016, ApJS, 223, 26
Ackermann, M., Ajello, M., Albert, A., et al. 2012, ApJS, 203, 4
Aharonian, F. A. 2000, New Astron., 5, 377
Aharonian, F., Akhperjanian, A. G., Bazer-Bachi, A. R., et al. 2006, A&A, 457, 899
Aharonian, F., Akhperjanian, A. G., Bazer-Bachi, A. R., et al. 2007, ApJ, 664, L71
Aharonian, F., Akhperjanian, A. G., Anton, G., et al. 2009, ApJ, 696, L150

---

[12] https://icecube.wisc.edu/science/data/PS-IC86-2011

Ansoldi, S., Antonelli, L. A., Arcaro, C., et al. 2018, ApJ, 863, L10
Atwood, W. B., Abdo, A. A., Ackermann, M., et al. 2009, ApJ, 697, 1071
Baloković, M., Paneque, D., Madejski, G., et al. 2016, ApJ, 819, 156
Band, D. L., & Grindlay, J. E. 1985, ApJ, 298, 128
Bernlöhr, K., Carrol, O., Cornils, R., et al. 2003, Astropart. Phys., 20, 111
Bhatta, G., Mohorian, M., & Bilinsky, I. 2018, A&A, 619, A93
Burrows, D. N., Hill, J. E., Nousek, J. A., et al. 2005, Space Sci. Rev., 120, 165
Cerruti, M., Zech, A., Boisson, C., & Inoue, S. 2015, MNRAS, 448, 910
Cerruti, M., Zech, A., Boisson, C., & Inoue, S. 2012, in 5th International Meeting
    on High Energy Gamma-Ray Astronomy, AIP Conf. Ser., 1505, 635
Cerruti, M., Zech, A., Boisson, C., et al. 2018, MNRAS, 483, L12
Chadwick, P. M., Lyons, K., McComb, T. J. L., et al. 1999, ApJ, 513, 161
Chen, L. 2017, ApJ, 842, 129
Chevalier, J., Sanchez, D. A., Serpico, P. D., Lenain, J.-P., & Maurin, G. 2019,
    MNRAS, 484, 749
Cutini, S. 2013, ATel, 4755
Cutini, S. 2014, ATel, 6148
de Naurois, M., & Rolland, L. 2009, Astropart. Phys., 32, 231
Dickey, J. M., & Lockman, F. J. 1990, ARA&A, 28, 215
Falomo, R., Pesce, J. E., & Treves, A. 1993, ApJ, 411, L63
Foreman-Mackey, D., Hogg, D. W., Lang, D., & Goodman, J. 2013, PASP, 125,
    306
Foschini, L., Ghisellini, G., Tavecchio, F., et al. 2007, ApJ, 657, L81
Foschini, L., Treves, A., Tavecchio, F., et al. 2008, A&A, 484, L35
Funk, S., Hermann, G., Hinton, J., et al. 2004, Astropart. Phys., 22, 285
Furniss, A., Noda, K., Boggs, S., et al. 2015, ApJ, 812, 65
Gao, S., Fedynitch, A., Winter, W., & Pohl, M. 2019, Nat. Astron., 3, 88
Gaur, H., Chen, L., Misra, R., et al. 2017, ApJ, 850, 209
Harrison, F. A., Craig, W. W., Christensen, F. E., et al. 2013, ApJ, 770, 103
H.E.S.S. Collaboration (Abramowski, A., et al.) 2013, A&A, 554, A72
H.E.S.S. Collaboration (Abdalla, H., et al.) 2017a, A&A, 598, A39
H.E.S.S. Collaboration (Abdalla, H., et al.) 2017b, A&A, 600, A89
Holler, M., Berge, D., van Eldik, C., et al. 2015, ArXiv e-prints
    [arXiv:1509.02902]
IceCube Collaboration (Aartsen, M. G., et al.) 2018, Science, 361, eaat1378
Kalberla, P. M. W., Burton, W. B., Hartmann, D., et al. 2005, A&A, 440, 775
Kataoka, J., Takahashi, T., Makino, F., et al. 2000, ApJ, 528, 243
Katarzynski, K., Lenain, J. P., Zech, A., Boisson, C., & Sol, H. 2008, MNRAS,
    390, 371
Keivani, A., Murase, K., Petropoulou, M., et al. 2018, ApJ, 864, 84
Liuzzo, E., Falomo, R., Treves, A., et al. 2013, AJ, 145, 73
Madejski, G. M., Nalewajko, K., Madsen, K. K., et al. 2016, ApJ, 831, 142
Madsen, K. K., Beardmore, A. P., Forster, K., et al. 2017, AJ, 153, 2
Mannheim, K. 1993, A&A, 269, 67
Mattox, J. R., Bertsch, D. L., Chiang, J., et al. 1996, ApJ, 461, 396
Mücke, A., & Protheroe, R. J. 2001, Astropart. Phys., 15, 121
Nelder, J., & Mead, R. 1965, Comput. J., 7, 308
Parsons, R. D., & Hinton, J. A. 2014, Astropart. Phys., 56, 26
Perlman, E. S., Madejski, G., Georganopoulos, M., et al. 2005, ApJ, 625, 727
Piron, F., Djannati-Atai, A., Punch, M., et al. 2001, A&A, 374, 895
Poole, T. S., Breeveld, A. A., Page, M. J., et al. 2008, MNRAS, 383, 627
Rybicki, G. B., & Lightman, A. P. 1986, Radiative Processes in Astrophysics
    (Germany: Wiley-VCH), 400
Sanchez, D. A., & Deil, C. 2013, in Proceedings of the 33rd International Cosmic
    Ray Conference (ICRC 2013)
Schlafly, E. F., & Finkbeiner, D. P. 2011, ApJ, 737, 103
Schwartz, D. A., Griffiths, R. E., Schwarz, J., Doxsey, R. E., & Johnston, M. D.
    1979, ApJ, 229, L53
The Fermi-LAT Collaboration 2020, ApJS, 247, 33
Urry, C. M., & Mushotzky, R. F. 1982, ApJ, 253, 38
Zhang, Y. H. 2008, ApJ, 682, 789

1 Centre for Space Research, North-West University, Potchefstroom 2520, South Africa
2 Universität Hamburg, Institut für Experimentalphysik, Luruper Chaussee 149, 22761 Hamburg, Germany
3 Max-Planck-Institut für Kernphysik, PO Box 103980, 69029 Heidelberg, Germany
4 Dublin Institute for Advanced Studies, 31 Fitzwilliam Place, Dublin 2, Ireland
5 High Energy Astrophysics Laboratory, RAU, 123 Hovsep Emin St, Yerevan 0051, Armenia
6 Yerevan Physics Institute, 2 Alikhanian Brothers St., 375036 Yerevan, Armenia
7 Institut für Physik, Humboldt-Universität zu Berlin, Newtonstr. 15, 12489 Berlin, Germany
8 University of Namibia, Department of Physics, Private Bag 13301, Windhoek 12010, Namibia
9 GRAPPA, Anton Pannekoek Institute for Astronomy, University of Amsterdam, Science Park 904, 1098, XH Amsterdam, The Netherlands
10 Department of Physics and Electrical Engineering, Linnaeus University, 351 95 Växjö, Sweden
11 Institut für Theoretische Physik, Lehrstuhl IV: Weltraum und Astrophysik, Ruhr-Universität Bochum, 44780 Bochum, Germany
12 Institut für Astro- und Teilchenphysik, Leopold-Franzens-Universität Innsbruck, 6020 Innsbruck, Austria
13 School of Physical Sciences, University of Adelaide, Adelaide 5005, Australia
14 LUTH, Observatoire de Paris, PSL Research University, CNRS, Université Paris Diderot, 5 place Jules Janssen, 92190 Meudon, France
15 Sorbonne Université, Université Paris Diderot, Sorbonne Paris Cité, CNRS/IN2P3, Laboratoire de Physique Nucléaire et de Hautes Energies, LPNHE, 4 place Jussieu, 75252 Paris, France
16 Laboratoire Univers et Particules de Montpellier, Université Montpellier, CNRS/IN2P3, CC 72, Place Eugène Bataillon, 34095 Montpellier Cedex 5, France
17 IRFU, CEA, Université Paris-Saclay, 91191 Gif-sur-Yvette, France
18 Astronomical Observatory, The University of Warsaw, Al. Ujazdowskie 4, 00-478 Warsaw, Poland
19 Aix Marseille Université, CNRS/IN2P3, CPPM, Marseille, France
20 Instytut Fizyki Jądrowej PAN, ul. Radzikowskiego 152, 31-342 Kraków, Poland
21 School of Physics, University of the Witwatersrand, 1 Jan Smuts Avenue, Braamfontein, Johannesburg 2050, South Africa
22 Laboratoire d'Annecy de Physique des Particules, Univ. Grenoble Alpes, Univ. Savoie Mont Blanc, CNRS, LAPP, 74000 Annecy, France
23 Landessternwarte, Universität Heidelberg, Königstuhl, 69117 Heidelberg, Germany
24 Université Bordeaux, CNRS/IN2P3, Centre d'Études Nucléaires de Bordeaux Gradignan, 33175 Gradignan, France
25 Institut für Astronomie und Astrophysik, Universität Tübingen, Sand 1, 72076 Tübingen, Germany
26 Laboratoire Leprince-Ringuet, École Polytechnique, CNRS, Institut Polytechnique de Paris, 91128 Palaiseau, France
27 APC, AstroParticule et Cosmologie, Université Paris Diderot, CNRS/IN2P3, CEA/Irfu, Observatoire de Paris, Sorbonne Paris Cité, 10 rue Alice Domon et Léonie Duquet, 75205 Paris Cedex 13, France
28 Univ. Grenoble Alpes, CNRS, IPAG, 38000 Grenoble, France
29 Department of Physics and Astronomy, The University of Leicester, University Road, Leicester LE1 7RH, UK
30 Nicolaus Copernicus Astronomical Center, Polish Academy of Sciences, ul. Bartycka 18, 00-716 Warsaw, Poland
31 Institut für Physik und Astronomie, Universität Potsdam, Karl-Liebknecht-Strasse 24/25, 14476 Potsdam, Germany
32 Friedrich-Alexander-Universität Erlangen-Nürnberg, Erlangen Centre for Astroparticle Physics, Erwin-Rommel-Str. 1, 91058 Erlangen, Germany
33 DESY, 15738 Zeuthen, Germany
34 Obserwatorium Astronomiczne, Uniwersytet Jagielloński, ul. Orla 171, 30-244 Kraków, Poland
35 Centre for Astronomy, Faculty of Physics, Astronomy and Informatics, Nicolaus Copernicus University, Grudziadzka 5, 87-100 Torun, Poland
36 Department of Physics, University of the Free State, PO Box 339, Bloemfontein 9300, South Africa

[37] Department of Physics, Rikkyo University, 3-34-1 Nishi-Ikebukuro, Toshima-ku, Tokyo 171-8501, Japan

[38] Kavli Institute for the Physics and Mathematics of the Universe (WPI), The University of Tokyo Institutes for Advanced Study (UTIAS), The University of Tokyo, 5-1-5 Kashiwa-no-Ha, Kashiwa, Chiba 277-8583, Japan

[39] Department of Physics, The University of Tokyo, 7-3-1 Hongo, Bunkyo-ku, Tokyo 113-0033, Japan

[40] RIKEN, 2-1 Hirosawa, Wako, Saitama 351-0198, Japan

[41] Now at Physik Institut, Universität Zürich, Winterthurerstrasse 190, 8057 Zürich, Switzerland

[42] Institut de Ciències del Cosmos (ICC UB), Universitat de Barcelona (IEEC-UB), Martí Franquès 1, 08028 Barcelona, Spain

[43] Kavli Institute for Particle Astrophysics and Cosmology, Department of Physics and SLAC National Accelerator Laboratory, Stanford University, Stanford, CA 94305, USA

[44] Cahill Center for Astronomy and Astrophysics, Caltech, Pasadena, CA 91125, USA

[45] California State University – East Bay, 25800 Carlos Bee Boulevard, Hayward, CA 94542, USA

[46] Yale Center for Astronomy and Astrophysics, Physics Department, Yale University, PO Box 208120, New Haven, CT 06520-8120, USA

[47] Department of Physics and Astronomy, Clemson University, Kinard Lab of Physics, Clemson, SC 29634-0978, USA

[48] Jet Propulsion Laboratory, California Institute of Technology, Pasadena, CA 91109, USA

[49] Space Science Laboratory, University of California, Berkeley, CA 94720, USA

[50] Center for Astrophysics | Harvard & Smithsonian, 60 Garden Street, Cambridge, MA 02138, USA

[51] Black Hole Initiative at Harvard University, 20 Garden Street, Cambridge, MA 02138, USA

[52] ASI Science Data Center, Via del Politecnico snc, 00133 Roma, Italy

[53] INAF – Osservatorio Astronomico di Roma, Via di Frascati 33, 00040 Monteporzio, Italy

[54] INAF – Osservatorio Astronomico di Brera, Via Bianchi 46, 23807 Merate, Italy

[55] Max-Planck-Institut fur Physik, 80805 Munchen, Germany